Biogeosciences Discuss., 9, 14013–14052, 2012
www.biogeosciences-discuss.net/9/14013/2012/
doi:10.5194/bgd-9-14013-2012

Biogeosciences Discussions

Marine denitrification rates determined from a global 3-dimensional inverse model

T. DeVries[1], C. Deutsch[1], P. A. Rafter[2], and F. Primeau[3]

[1]Department of Atmospheric and Oceanic Sciences, University of California Los Angeles, Los Angeles, CA, 90095, USA
[2]Department of Geosciences, Princeton University, Princeton, NJ, 08544, USA
[3]Department of Earth System Science, University of California Irvine, Irvine, CA, 92697, USA

Received: 28 August 2012 – Accepted: 29 August 2012 – Published: 12 October 2012

Correspondence to: T. DeVries (tdevries@atmos.ucla.edu)

Published by Copernicus Publications on behalf of the European Geosciences Union.

Abstract

A major impediment to understanding long-term changes in the marine nitrogen (N) cycle is the persistent uncertainty about the rates, distribution, and sensitivity of its largest fluxes in the modern ocean. We use a global 3-dimensional ocean circulation model to obtain the first estimate of marine denitrification rates that is maximally consistent with available observations of nitrate deficits and the nitrogen isotopic ratio of ocean nitrate. We find a global rate of marine denitrification in suboxic waters and sediments of 120–240 $\mathrm{Tg\,N\,yr^{-1}}$, which is lower than most other recent estimates. The difference stems from the ability to represent the 3-D spatial structure of suboxic zones, where denitrification rates of 50–77 $\mathrm{Tg\,N\,yr^{-1}}$ result in up to 50 % depletion of nitrate. This depletion reduces the effect of local isotopic enrichment on the rest of the ocean, allowing the N isotope ratio of oceanic nitrate to be achieved with a sedimentary denitrification rate about 1.3–2.3 times that of suboxic zones. This balance of N losses between sediments and suboxic zones is shown to obey a simple relationship between isotope fractionation and the degree of nitrate consumption in the core of the suboxic zones. The global denitrification rates derived here suggest that the marine nitrogen budget is likely close to balanced.

1 Introduction

Relative to the cycles of other biologically important nutrients, the marine nitrogen cycle is potentially highly dynamic, with large input and output rates and a relatively short turnover time. A question of central importance is whether the marine nitrogen budget can sustain long-term imbalances, or if the primary sources and sinks of nitrogen are closely coupled by self-stabilizing feedbacks, preventing significant variability in the ocean's nitrogen inventory. The answer remains unclear in large part because the nitrogen budget of the contemporary ocean is poorly constrained, primarily due to uncertainty in the rate of nitrogen loss due to denitrification, by which fixed nitrogen is

BGD
9, 14013–14052, 2012

converted to N_2 gas and lost from the ocean. Estimates of denitrification rates in the contemporary ocean range from about 200 $Tg\,N\,yr^{-1}$ (Gruber and Sarmiento, 1997, 2002; Gruber, 2008) to over 400 $Tg\,N\,yr^{-1}$ (Middelburg et al., 1996; Codispoti et al., 2001; Brandes and Devol, 2002; Codispoti, 2007).

Denitrification occurs both in small areas of the ocean where waters become suboxic (water-column denitrification), and in the pore-waters of sediments throughout the ocean (benthic denitrification). Recent work suggests that the rate of water-column denitrification is about 60–70 $Tg\,N\,yr^{-1}$ (DeVries et al., 2012), but the rate of benthic denitrification remains poorly known. Direct measurements of denitrification rates in sediments have been made at a handful of sites (e.g. Devol and Christensen, 1993; Devol et al., 1997; Laursen and Seitzinger, 2002; Rao et al., 2007), but scaling these up to a global estimate is precluded by the sparsity of observations and the spatial and temporal variability in these rates.

One solution to the challenge of deriving a global estimate of marine denitrification rates is to make use of observed marine nitrate (NO_3) deficits and nitrogen isotopic ratios (Fig. 1). These quantities are more widely measured than denitrification rates, and tend to reflect the integrated effects of highly variable denitrification processes. Nitrate deficits can be measured by the N^* tracer, which reflects the difference between the in-situ NO_3 concentration and that expected due to the average nitrate to phosphate (PO_4) ratio of organic matter, $N^* = NO_3 - 16 \times PO_4$. The isotopic ratio of ^{15}N to ^{14}N in oceanic nitrate is commonly expressed as $\delta^{15}NO_3 = (^{15}NO_3/^{14}NO_3 - 1) \times 1000$.

In tandem, N^* and $\delta^{15}NO_3$ provide powerful constraints on marine denitrification rates. Denitrification in both the water-column and the sediments consumes nitrate but not phosphate, imparting a negative signature to N^*. The influence of denitrification is clearly visible in the thermocline N^* distribution, which shows strongly negative N^* due to water-column denitrification in suboxic waters of the Arabian Sea and the Eastern Tropical Pacific, and negative N^* due to benthic denitrification in the sub-Arctic Pacific and elsewhere (Fig. 1b). Water-column denitrification preferentially removes the lighter nitrogen isotope, and imparts a heavy isotopic signature of about $\epsilon_w = 25‰$ (Barford

BGD
9, 14013–14052, 2012

et al., 1999) to surrounding waters, which explains the elevated $\delta^{15}NO_3$ values in the suboxic waters of the Eastern Tropical Pacific and the Arabian Sea (Fig. 1d). On the other hand, benthic denitrification has a much lighter isotopic signature of $0‰ \leq \epsilon_b \lesssim 3‰$ (Brandes and Devol, 1997, 2002; Lehmann et al., 2004, 2007), as evidenced by the lack of isotopic enrichment in the sub-Arctic Pacific (e.g. Yoshikawa et al., 2006) (Fig. 1d).

The mean ocean $\delta^{15}NO_3$ of about 5‰ primarily reflects a balance between the input of isotopically light NO_3 by nitrogen fixers (with an isotopic signature of $-2‰ \lesssim \epsilon_{fix} \leq 0‰$; Macko et al., 1987; Carpenter et al., 1997) and a mixture of water-column and benthic denitrification, and therefore provides a strong constraint on the relative amounts of denitrification occurring in the water-column (W) and the sediments (B), which can be expressed compactly as the ratio B/W. Simple geochemical box models have been used to derive estimates of B/W, but these estimates still yield a large uncertainty of $1 < B/W < 4$ (Brandes and Devol, 2002; Deutsch et al., 2004; Altabet, 2007). The uncertainty in B/W partly reflects uncertainty in isotopic enrichment factors and the isotopic ratio of organic nitrogen (Brandes and Devol, 2002; Altabet, 2007). More importantly however, the wide range of estimates of B/W reflects inaccuracies associated with simple box models which cannot resolve important spatial features of the ocean circulation and denitrification processes. In order to correctly account for the isotopic effects of nitrate consumption in the suboxic water-column, a model should correctly simulate the degree of nitrate consumption in suboxic zones, and accurately simulate how the suboxic zones are ventilated and how tracers are exchanged between the suboxic and oxic ocean (e.g. Deutsch et al., 2004). These latter effects can only be accurately captured in a spatially explicit 3-dimensional ocean circulation model. The only previous study to simulate nitrogen isotopes in a global ocean circulation model suffered from severe over-consumption of nitrate in the suboxic water-column (Somes et al., 2010), rendering the B/W estimate from that model innacurate.

Here we address these issues by coupling a simple nitrogen cycle model to a data-constrained ocean circulation model (Sect. 2.1). The parameters of the nitrogen cycle

BGD
9, 14013–14052, 2012

model are iteratively adjusted using an adjoint approach to achieve an optimal fit to the observed distributions of N^* and $\delta^{15}NO_3$ (Sects. 2.2 and 2.3). The solution found by this global inverse nitrogen cycle model is used to estimate the global rates and patterns of water-column and benthic denitrification (Sect. 3). The effects of denitrification on the N^* distribution (Sect. 4.1) and on the mean ocean $\delta^{15}NO_3$ (Sect. 4.2) are discussed. Model parameters that are poorly constrained by the available data are varied by a Monte Carlo procedure in order to derive uncertainty estimates on denitrification rates (Sect. 4.3). We also discuss the implications of our findings for the global marine nitrogen budget (Sect. 5).

2 A global inverse nitrogen cycle model

2.1 Circulation model and nitrogen cycle model

The physical component of the nitrogen cycle model is based on the data-constrained model of DeVries and Primeau (2011), which has been extended to increase the resolution of the model to 2° in the horizontal, with 24 vertical levels. As in DeVries and Primeau (2011), the circulation of the model has been tuned to closely reproduce the observed temperature, salinity, and radiocarbon distributions in the ocean using an adjoint method. We also add a simple simulation (Najjar and Orr, 1998) of the phosphate and dissolved organic phosphate (DOP) cycle to the model, and add the observed PO_4 distribution (Garcia et al., 2010a) as an additional constraint on the circulation and biological fluxes in the model. Unlike the study of DeVries et al. (2012), we do not assimilate CFC-11 observations in this version of the model.

The circulation determined in the above step is then taken offline and used to drive the physical tracer transport in a simple marine nitrogen cycle model. The internal cycling of N is driven by restoring surface nitrate toward observed distributions, as done for PO_4. This assures that the model reproduces the observed nutrient stoichiometry (N^*) of surface waters. One of the necessary chemical signatures of N_2 fixation

BGD
9, 14013–14052, 2012

– a non-Redfield uptake of NO_3 and PO_4 – is therefore already implicit in the model design. Thus the model cannot simultaneously solve for the spatial distribution of N_2 fixation. Its rates and pattern are used solely to close the N budget. An inverse solution that includes this term requires an explicit treatment of non-Redfield stoichiometry of nutrient uptake, as well as atmospheric N deposition, and is left for a future study.

Water-column denitrification in the model occurs where observed oxygen concentrations fall below a critical threshold $O_{2,crit}$. Observed oxygen concentrations are taken from the 2009 World Ocean Atlas monthly climatology (Garcia et al., 2010b) after correcting for measurements in low-oxygen regions following the method of Bianchi et al. (2012). Benthic denitrification occurs within grid cells that have some contact with the ocean floor. The grid cells having contact with the ocean floor are determined by interpolating observed ocean floor bathymetry to the model grid, as described in Appendix A. Water-column denitrification rates are proportional to the rate of organic matter remineralization within suboxic zones, while benthic denitrification rates are proportional to the rate of organic matter supply to the sediments, and also depend on bottom-water nitrate and oxygen concentrations. Denitrification in the water-column and sediments is balanced by nitrogen fixation, with a rate that depends on local surface NO_3 concentrations, temperature, light levels, and iron supply. Production of organic nitrogen is parameterized by restoring to observed NO_3 in the top two model layers (above 73 m depth). Organic nitrogen is exported out of the surface layers as either dissolved organic nitrogen (DON) which remineralizes with first-order kinetics, or as particulate organic nitrogen (PON) which remineralizes according to a power-law dependence on depth (Martin et al., 1987). See Appendix A for a full description of the nitrogen cycle model.

2.2 Inverse nitrogen cycle model

The parameters of the nitrogen cycle model include the critical oxygen threshold for water-column denitrification; the ratio of nitrate consumed to organic matter remineralized during water-column denitrification, and that during benthic denitrification; the

BGD
9, 14013–14052, 2012

oxygen and nitrate dependence of benthic denitrification; the isotopic enrichment factors for nitrogen fixation, water-column denitrification, benthic denitrification, and uptake of nitrate to form organic nitrogen; the maximum nitrogen fixation rate as well as its temperature, light, nitrate, iron, and depth dependence; the fraction of organic matter production routed to the dissolved organic nitrogen (DON) pool; and the decay timescale for DON. Most of the model parameters can be constrained by the N^* and $\delta^{15}NO_3$ data, and these parameters (Table B1) are iteratively adjusted using an adjoint method to find the set of parameters that allows the model to best fit observed N^* and $\delta^{15}NO_3$ (Fig. 1). The optimal parameter set is the solution to the inverse model. See Appendix B for a full description of the inverse model.

We withhold four of the model parameters from the inversion because they are likely to be unconstrained by the available N^* and $\delta^{15}NO_3$ data. Primarily due to the sparsity of the $\delta^{15}NO_3$ observations, only one of the isotopic enrichment factors can be constrained independently of the others. We solve for ϵ_w as part of the solution to the inverse model, since there is good data coverage in the suboxic zones where water-column denitrification occurs (Fig. 1c). We fix the isotopic enrichment factor for uptake of nitrate to form organic matter (ϵ_{up}) at 5‰ as in Somes et al. (2010). We account for uncertainty in the remaining isotopic fractionation factors by re-running the inverse model with various combinations of ϵ_b (0, 1, 2, or 3‰) and ϵ_{fix} (−2, −1, or 0‰). The fraction of organic nitrogen routed to the DON pool (σ_{DON}) is also poorly constrained, since observations of DON concentrations are not used to constrain the model. So we also vary the value of σ_{DON} over a wide range (σ_{DON} = 1/4, 1/3, 1/2, or 2/3) in different versions of the inverse model. In all, the different combinations of ϵ_w, ϵ_{fix}, and σ_{DON} produce 48 configurations for the inverse model. The uncertainty ranges quoted below represent the full range of optimal model solutions under each of these 48 different model configurations.

Data constraints for the inverse model include N^* concentrations derived from the 2009 World Ocean Atlas objectively mapped annual mean NO_3 and PO_3 data (Garcia et al., 2010a), which are interpolated to the model grid, and $\delta^{15}NO_3$ observations

BGD
9, 14013–14052, 2012

compiled from the literature (Somes et al., 2010; Rafter et al., 2012; De Pol Holz et al., 2009; Liu, 1979; DiFiore et al., 2009; Yoshikawa et al., 2005, 2006, P. Rafter and D. Sigman, unpublished data) which are binned to the model grid. We exclude $\delta^{15}NO_3$ observations above 200 m depth, due to numerical noise in the simulated $\delta^{15}NO_3$ fields that can occur near the surface where nitrate concentrations are very low (close to zero).

2.3 Model-data comparison

The optimization procedure produces a good fit to the observed distributions of N^* (Fig. 2b) and $\delta^{15}NO_3$ (Fig. 2c). Although NO_3 is not included in the cost function measuring model-data misfit, a good fit to observed NO_3 (Fig. 2a) is achieved by virtue of the fact that both PO_4 and N^* are included in the cost function. The mean modeled nitrate and N^* concentrations are slightly lower than the observed values, and the mean ocean $\delta^{15}NO_3$ is around 5 ‰, in excellent agreement with the observations. The model also demonstrates good agreement with the observed degree of nitrate consumption ($f_c = 1 - NO_3/16PO_4$) and $\delta^{15}NO_3$ in low-oxygen zones (Fig. 2d). The degree of nitrate consumption in waters with less than 20 µM O_2 in the model is between 0.1–0.5, in agreement with observations. At high degrees of nitrate consumption ($f_c \sim 0.4$), the modeled $\delta^{15}NO_3$ is about 12–16 ‰, depending on the oceanic region. This agrees with the mean observed $\delta^{15}NO_3$ in these regions, although the observations show more scatter than the modeled values. This could be due to seasonal, interannual and eddy variability not captured by the large-scale steady-state circulation model, or to variability in isotopic fractionation and in the N : P ratio of organic matter that is not captured by the simple nitrogen cycle model.

The model also matches the depth distribution of N^* and $\delta^{15}NO_3$ in both the Atlantic and Indo-Pacific basins quite well (Fig. 3). Depth profiles of modeled and observed $\delta^{15}NO_3$ in the Atlantic show that the model does not produce quite low enough $\delta^{15}NO_3$ near the surface, nor is the thermocline maximum as strong as observed (Fig. 3a). Atmospheric deposition, which is not accounted for in the model, may play an important

BGD
9, 14013–14052, 2012

role in determining the shallow nitrate $\delta^{15}NO_3$ in the Atlantic (Knapp et al., 2008). Deep ocean values in the Atlantic are slightly lower than observed, but the observations lie within the envelope of model uncertainty. The modeled depth profile of $\delta^{15}NO_3$ in the Indo-Pacific basin matches the observations fairly well throughout the water column (Fig. 3a). The greatest mismatch occurs above 500 m, where modeled $\delta^{15}NO_3$ is lower than observed. This could potentially indicate too little N fixation in the model in regions with $\delta^{15}NO_3$ observations, primarily suboxic zones. N^* concentrations in the Atlantic basin show a general decrease with depth in both the model and the observations (Fig. 3b). The model does produce a thermocline maximum in N^* in the Atlantic, although not as pronounced as observed. Except in the deepest Atlantic, where the model slightly under-predicts N^*, the observed mean N^* lies within the model-predicted uncertainty. The model matches the general magnitude and shape of the observed N^* depth profile in the Indo-Pacific, with some distinctive differences most notably in the depth range 500–1000 m where the model has a stronger and shallower negative N^* peak than the observations, and in the deep ocean where the model N^* is more negative than observed (Fig. 3b). However, the largest model-data misfit ($\sim 1\,\mu M$) is small compared to the N^* signature of denitrification (see for example Fig. 5a and discussion below).

3 Denitrification rates and their global distribution

The global distribution of water-column and benthic denitrification (Fig. 4) was determined from the optimal solution under each of the 48 different model configurations. Water-column denitrification is confined primarily to low-oxygen zones in the Eastern Tropical North and South Pacific, and in the Arabian Sea (Fig. 4a). Small (negligible) amounts of water-column denitrification occur in the sub-Arctic Pacific and in the Bay of Bengal. Globally, the rate of water-column denitrification predicted by the model is 50–76 $Tg\,N\,yr^{-1}$ (Table 1). Of this total, 9–14 $Tg\,N\,yr^{-1}$ is due to denitrification in the Arabian Sea, and 41–63 $Tg\,N\,yr^{-1}$ is due to denitrification in the Eastern Tropical Pacific

BGD
9, 14013–14052, 2012

(Table 1). These rates agree, within their uncertainty, with an estimate that used nitrogen gas observations from within suboxic zones to constrain water-column denitrification rates (DeVries et al., 2012).

Benthic denitrification rates are highest in highly productive coastal upwelling regions (e.g. the Eastern Tropical Pacific, West African coast, and Arabian Sea), and in regions of shallow continental shelves (e.g. the sub-Arctic Pacific, Northeast North America, Indonesian Archipelago, Arctic margin, and Southeastern South America) (Fig. 4b). These areas experience benthic denitrification rates over 100 times greater than rates typical of deep ocean sediments. Globally, the model predicts that 70–170 $\mathrm{Tg\,N\,yr^{-1}}$ of benthic denitrification is needed to match the constraints provided by the N^* and $\delta^{15}NO_3$ data, with the largest contribution from sediments in the Pacific Ocean (Table 1).

The vertical distribution of water-column denitrification is highly concentrated, with almost all denitrification occurring above 1000 m depth, coincident with the depth of suboxic zones (Fig. 4c). Water-column denitrification rates have a shallower peak than the suboxic volume (Fig. 4c) due to the fact that organic matter remineralization rates decrease with depth. Benthic denitrification also has a shallow peak, with highest rates above 1000 m depth, although approximately half of benthic denitrification occurs below 1000 m (Fig. 4d). The primary factor controlling the distribution of benthic denitrification is the rate at which organic matter is delivered to the sediments. However, there is a mid-depth peak in benthic denitrification at about 1000–2000 m that is not found in the rate of organic nitrogen supply to the sediments (Fig. 4d). This is due to enhanced benthic denitrification rates under low oxygen and high nitrate conditions, an effect also found in a previous modeling study (Middelburg et al., 1996).

The rates of benthic denitrification reported here are lower than previous model-based estimates that were not constrained by observed nitrate deficits or nitrate isotopes, which yield estimates of about 250–300 $\mathrm{Tg\,N\,yr^{-1}}$ (Middelburg et al., 1996; Seitzinger et al., 2006). A more recent estimate (Bianchi et al., 2012), based on the meta-model parameterization of Middelburg et al. (1996) and using satellite-derived

BGD
9, 14013–14052, 2012

estimates of sinking organic matter flux, inferred a benthic denitrification rate of $182 \pm 55\,\mathrm{Tg\,N\,yr^{-1}}$, which agrees within uncertainty with the rate estimated here.

A significant difference between this study and previous studies is that our model predicts that only about 20 % of benthic denitrification occurs in shelf sediments (< 160 m depth), in contrast with other estimates suggesting 35–70 % of benthic denitrification occurs on continental shelves (Middelburg et al., 1996; Bianchi et al., 2012). Although we have used a parameterization to account for the presence of shallower continental shelves than are resolved by the model's bottom topography (see Appendix A), the model resolution is still insufficient to resolve the enhanced biological productivity and high organic carbon export rates within those regions. Therefore the actual rate of benthic denitrification on continental shelves may be higher than reported here. Nonetheless, the mean ocean $\delta^{15}NO_3$ constraint, which is satisfied by the model, requires that if benthic denitrification on continental shelves is greater than predicted by the model, it must be balanced by input of nitrate of a similar isotopic composition. This additional input of nitrate could be supplied by rivers, which are estimated to dump about $30\,\mathrm{Tg\,N\,yr^{-1}}$ into coastal waters (Gruber and Galloway, 2008), with an isotopic enrichment of about 4 ‰ (Brandes and Devol, 2002). An additional $30\,\mathrm{Tg\,N\,yr^{-1}}$ of denitrification in shelf sediments would raise the fraction of benthic denitrification occurring on continental shelves to about 40 %, more in line with previous estimates. However, even with such an additional amount of benthic denitrification, the global marine benthic denitrification rate estimated here is less than most other model estimates.

4 Discussion

4.1 Effect of denitrification on vertical N^* distribution

Water-column and benthic denitrification have distinct effects on the vertical distribution of N^* in the ocean. To estimate the effect of denitrification on N^*, we simulate an idealized tracer that is produced at a rate of 1 mol tracer (1 mol NO_3 consumed by

BGD
9, 14013–14052, 2012

denitrification)$^{-1}$. The tracer is immediately removed from the ocean when it reaches the top model layer, where all nutrients are considered "preformed". We perform separate calculations for benthic and water-column denitrification. For comparison with the study of Anderson and Sarmiento (1994), we calculate the average amount of tracer on isopycnal horizons (below 400 m depth) and plot the results as a function of the average depth of each isopycnal horizon (Fig. 5a). The results show that N^* due to water-column denitrification reaches a minimum in the thermocline at about 700–800 m depth, with a peak value of around −1 µM (Fig. 5a). Benthic denitrification produces an N^* profile with a mid-depth peak of about −3 to −4 µM at 1500–3000 m depth (Fig. 5a). These are the globally averaged effects of denitrification; the effect is about 50 % larger in the Indo-Pacific basin where most denitrification occurs and where waters are older, allowing for accumulation of reaction products.

We also calculated the nitrogen to phosphorus (N : P) ratio of remineralized organic matter in the interior ocean in the model following a procedure similar to that of Anderson and Sarmiento (1994). The amount of "preformed" nitrate (or phosphate) in the interior ocean is calculated from an idealized tracer with a surface concentration equal to the modeled surface concentration, and no sources or sinks in the interior ocean. The amount of remineralized nitrate (or phosphate) is then determined by subtracting the preformed component from the total concentration. We determine the N : P ratio of remineralized organic matter from a linear regression of remineralized nitrate against remineralized phosphate along the same isopycnal horizons used in Fig. 5a. Similar to the results of Anderson and Sarmiento (1994), we see that the near-surface N : P ratio calculated in this way is close to that of "fresh" organic matter (∼ 16 : 1), but drops to a minimum in the depth range 1500–3000 m (Fig. 5b). Anderson and Sarmiento (1994) hypothesized that the actual N : P ratio of remineralized organic matter was approximately constant with depth, but that the mid-depth minimum may be an artifact of benthic denitrification. By adding back in the remineralized NO_3 that is lost due to denitrification (Fig. 5a) and repeating the calculation, we find that indeed the N : P ratio of remineralization is approximately constant with depth (Fig. 5b), which is consistent with

BGD
9, 14013–14052, 2012

the original hypothesis of Anderson and Sarmiento (1994). The deepest isopycnals in Fig. 5b are associated with deep Labrador Sea water in the Western North Atlantic, a small region in which production is clearly non-Redfieldian.

4.2 Controls on the partitioning between benthic and water-column denitrification

We find a median value of $B/W = 1.7$ in our suite of optimized models, with a range of $1.3 < B/W < 2.3$ (Table 1). This significantly reduces the uncertainty on B/W over that derived from geochemical box models, which gave a range of $1 < B/W < 4$ (Brandes and Devol, 2002; Deutsch et al., 2004; Altabet, 2007). The relatively low value of B/W determined in this study contrasts with results expected from a linear isotope mass balance model (Brandes and Devol, 2002) which predicts the following relationship for B/W,

$$\frac{B}{W} = \frac{\epsilon_w - \delta + \epsilon_{fix}}{\delta - \epsilon_{fix} - \epsilon_b}, \quad (1)$$

where $\delta \approx 5‰$ is the mean nitrogen isotopic ratio of oceanic nitrate, and a balance between inputs by nitrogen fixation and removal by benthic and water-column denitrification is assumed. If both $\epsilon_{fix} = 0‰$ and $\epsilon_b = 0‰$, Eq. (1) predicts $B/W = 4$. However, the global inverse model predicts that B/W is about 1.9 in this case. This is because the impact of isotopic fractionation associated with water-column denitrification is diminished by the degree of nitrate consumption in suboxic zones (Deutsch et al., 2004). We find that the modeled B/W ratio can be explained much better (Fig. 6) by applying a simple correction to Eq. (1) to account for the degree of nitrate consumption (f_c) in suboxic zones

$$\frac{B}{W} = \frac{(1 - f_c)\epsilon_w - \delta + \epsilon_{fix}}{\delta - \epsilon_{fix} - \epsilon_b}. \quad (2)$$

BGD
9, 14013–14052, 2012

To apply Eq. (2) to our model results, we calculate f_c as the average of $(1 - NO_3/16PO_4)$ in the core of the suboxic zones (where observed O_2 is less than $O_{2,crit}$), and $\delta = (\overline{^{15}NO_3}/\overline{NO_3} - 1) \times 1000$, where the bar indicates the whole ocean average. For the model, we get $\delta = 5.4$‰ (range 5.2–5.7‰) and $f_c = 0.34$ (range 0.32–0.37).

This empirical relationship suggests that if there is complete consumption of nitrate in suboxic zones ($f_c = 1$), then the isotopic enrichment effect of water-column denitrification does not affect the mean ocean $\delta^{15}NO_3$. In fact the full effect of the isotopic enrichment due to water-column denitrification can never be achieved, because $f_c > 0$ whenever there is any water-column denitrification. In the model, the average f_c within suboxic zones of about 0.34 effectively reduces the enrichment factor for water-column denitrification from about 25‰ to about 17‰. The modeled f_c in suboxic zones agrees well with the observed average $f_c = 0.31$ within those same locations.

Equation (2) slightly overpredicts B/W by about 0.15 on average, primarily because Eq. (2) does not take into account the isotopic enrichment during the assimilation of nitrate to form organic matter. To obtain the magnitude of this effect we re-ran the model with $\epsilon_{up} = 0$‰ and all other parameters fixed at their values determined by the inversion process. The results show that the fractionation associated with nitrate assimilation lowers the mean ocean $\delta^{15}NO_3$ by about 0.5‰ on average (minimum of 0.3‰ and maximum of 1.2‰ in all the model runs). Taking uptake fractionation into account, by replacing δ in Eq. (2) by the value of δ in the case that $\epsilon_{up} = 0$‰, leads to a prediction that slightly underestimates the modeled B/W by about 0.15 on average. Equation (2) is therefore accurate within about ±0.15, depending on the value of ϵ_{up} and on the actual value of B/W. Remaining discrepancies between the value of B/W predicted by Eq. (2) and that determined by the model are likely due to the inadequacy of using a single value of f_c to account for the spatially heterogeneous effects of water-column denitrification.

These results emphasize the importance of simultaneously achieving good fits to both nitrate deficits (to get f_c correct) and nitrogen isotopes (to get δ correct) in order

BGD
9, 14013–14052, 2012

to derive a good estimate of marine denitrification rates. Using only one or the other constraint can produce misleading results. For example, a box model that was tuned to fit mean ocean $\delta^{15}NO_3$ but not N^* found a value of $B/W \sim 4$ (Brandes and Devol, 2002) because it did not take into account the effects of nitrate consumption in suboxic zones, while an ocean circulation model that was tuned to fit mean ocean $\delta^{15}NO_3$ but not N^* found a value of $B/W \sim 0.5$ (Somes et al., 2010), because the modeled f_c was too large.

4.3 Uncertainty on denitrification rates

The globally integrated rate of marine denitrification predicted by the model ranges from about 120–240 $Tg\,N\,yr^{-1}$, with a median rate of 170 $Tg\,N\,yr^{-1}$ (Table 1). We find that uncertainty in the isotopic enrichment factors (ϵ_{fix} and ϵ_b) and uncertainty in the fraction of organic matter production routed to the DON pool (σ_{DON}) contribute approximately equally to the uncertainty in the globally integrated denitrification rate (Figs. 7a, c). Denitrification rates generally increase with larger values of ϵ_b and ϵ_{fix} (Fig. 7a). This relationship follows because for larger values of ϵ_b or ϵ_{fix}, a larger B/W ratio is needed to achieve a mean ocean $\delta^{15}NO_3$ of ~ 5‰ (Fig. 7b), which is achieved in the model by increasing benthic denitrification rates. It is also the case that B/W increases with smaller σ_{DON} values (Fig. 7d). This is because with smaller σ_{DON} values a larger fraction of particulate organic matter sinks out of the euphotic zone, and therefore there is a larger supply of organic matter to the sediments.

Interestingly, we find that the ratio B/W is relatively well constrained despite large uncertainties in the isotopic enrichment factors. This is because in the inverse model, the fractional consumption f_c in suboxic zones generally increases slightly with increasing values of ϵ_b or ϵ_{fix}, while ϵ_w decreases with increasing values of ϵ_b or ϵ_{fix}. Both of these effects reduce the sensitivity of B/W to the isotopic enrichment factors for fixation and benthic denitrification.

The effects of the N^* and $\delta^{15}NO_3$ constraints on the ratio of B/W predicted by the model can be illustrated by comparing the relative model-data misfit for each

BGD
9, 14013–14052, 2012

observational constraint as a function of B/W. The results for one particular model configuration show that the value of B/W needed to optimally match only the observed N^* is about 1.4, while that needed to optimally match only the observed $\delta^{15}NO_3$ is about 2.3 (Fig. 8). When both constraints are used, the model strikes a compromise between the two constraints such that the optimal value of B/W is about 1.8 (Fig. 8). In this particular model configuration, N^* provides the stronger constraint on B/W, as evidenced by the deeper minimum associated with the relative model-data misfit. This is owing to both the larger number of N^* observations compared to $\delta^{15}NO_3$ observations, and the fact that N^* generally shows a stronger sensitivity to changes in B/W (holding all other model parameters fixed) than does $\delta^{15}NO_3$.

The fact that the N^* and $\delta^{15}NO_3$ constraints require different optimal B/W values is not surprising, given uncertainties in the model parameters and imperfections inherent in representing complex phenomena with simple parametric equations, as well as uncertainties in the data. Only with perfect data and a perfect model could we expect the model to match both data sets optimally with the same set of parameters. This further illustrates the importance of bringing together both the N^* and $\delta^{15}NO_3$ data as constraints on denitrification rates, as long as one deals with imperfect models and imperfect data (which is always the case). Furthermore, the advantage of the inverse model is that uncertainties are explicitly coded into the model in terms of the adjustable control parameters, and the model is given freedom to choose between different parameter values in order to optimally match the observed N^* and $\delta^{15}NO_3$.

5 Implications and conclusions

The results of this study suggest that the marine nitrogen budget is unlikely to be strongly out of balance. Previous studies suggesting that marine denitrification rates are much higher than the rate of fixed nitrogen inputs depended on having either a very high rate of water-column denitrification, exceeding 90 $Tg\,N\,yr^{-1}$, and/or a large value of the ratio of benthic to water-column denitrification (B/W), exceeding 3 (Codispoti

BGD
9, 14013–14052, 2012

et al., 2001; Codispoti, 2007). Here we have shown that neither of these possibilities is likely, given the constraints provided by observed nitrate deficits (N^*) and nitrogen isotopic ratios of oceanic nitrate ($\delta^{15}NO_3$).

Results of our inverse model simulations suggest that the optimal rate of water-column denitrification needed to match the observed N^* and $\delta^{15}NO_3$ is about 60 (range of 50–77) $Tg\,N\,yr^{-1}$, in good agreement with a previous estimate based on N_2 gas measurements (DeVries et al., 2012). Meanwhile, the optimal value of B/W is about 1.7 (range 1.3–2.3). These are the first such estimates from a spatially explicit 3-dimensional ocean circulation model that is consistent with observed nitrate deficits and isotopic ratios. These estimates represent a significant improvement over previous estimates from box models (Brandes and Devol, 2002; Deutsch et al., 2004; Altabet, 2007), which could not resolve the 3-dimensional ocean circulation and the spatial variability in denitrification rates.

While the denitrification rates estimated here significantly reduce the uncertainty on the global rate of N loss from the ocean, some significant uncertainties in the marine N cycle remain that cannot be addressed using the present model. Perhaps most importantly, we have not addressed the magnitude and distribution of N fixation rates. A modeling study that used surface N^* distributions to estimate nitrogen fixation rates found a global N fixation rate of about 140 $Tg\,N\,yr^{-1}$ (Deutsch et al., 2007), while a recent observational study suggests that the global rate of N fixation is about 180 $Tg\,N\,yr^{-1}$ (Grosskopf et al., 2012), which is approximately equal to the mean global denitrification rate found in this study. However, it is not known precisely what amount of fixation is supported by the N^* and $\delta^{15}NO_3$ data in our model. This is because the information contained in the surface N^* distribution, which can in principle be used to constrain rates and patterns of nitrogen fixation (e.g. Deutsch et al., 2007), has already been absorbed by the surface restoring condition used to simulate the production of organic phosphorus and organic nitrogen. Furthermore, we do not use the surface $\delta^{15}NO_3$ data to constrain the solution (as mentioned above), nor do we simulate atmospheric

BGD
9, 14013–14052, 2012

nitrogen inputs, which could have significant local impacts on surface N^* and $\delta^{15}NO_3$ distributions (e.g. Hansell et al., 2007; Knapp et al., 2008).

In the future it will be important to jointly optimize for the rate of fixation and denitrification in the ocean, in order to reduce uncertainty on the magnitude of both fluxes. This will require making use of all of the available N^* and $\delta^{15}NO_3$ data, along with perhaps N_2 data as well, and will require simulating atmospheric and riverine N inputs that were not considered here. The inverse model framework developed here, with some modifications, will be a useful tool for such studies.

Appendix A

Nitrogen cycle model description

The governing equations for nitrate (NO_3) and dissolved organic nitrogen (DON) are

$$\frac{\partial NO_3}{\partial t} = \mathbf{A}NO_3 - \boldsymbol{J}_{prod} + \boldsymbol{J}^{wc}_{rem} + \boldsymbol{J}^{sed}_{rem} + \boldsymbol{J}^{NO_3}_{fix} - \boldsymbol{J}_{wcd} - \boldsymbol{J}_{sd} + \frac{1}{\tau_{DON}}DON \quad \text{(A1)}$$

$$\frac{\partial DON}{\partial t} = \left(\mathbf{A} - \frac{1}{\tau_{DON}}\right)DON + \sigma_{DON}\boldsymbol{J}_{prod} + \boldsymbol{J}^{DON}_{fix} \quad \text{(A2)}$$

where the linear operator **A** represents the model's discretized advection-diffusion transport operator, and τ_{DON} is a decay timescale for DON. The other sources and sinks are non-linear and are described below.

Production of organic nitrogen ($\boldsymbol{J}_{prod}$) in the euphotic zone represents a sink of nitrate and is parameterized by restoring to mean annual observed NO_3 (Garcia et al., 2010a) above $z_c = -73$ m (corresponding to the top two model layers) with a restoring

BGD
9, 14013–14052, 2012

timescale τ_b = 30 days,

$$J_{\text{prod}}(x,y,z) = \frac{1}{\tau_b}(NO_3 - NO_{3,\text{obs}}), \quad NO_3 > NO_{3,\text{obs}} \tag{A3}$$

$$J_{\text{prod}}(x,y,z) = 0, \quad NO_3 \le NO_{3,\text{obs}}, z < z_c. \tag{A4}$$

Of the total production of organic N, a fraction σ_{DON} is routed to the DON pool, and the remainder $(1-\sigma_{\text{DON}})$ to particulate organic nitrogen (PON). PON is remineralized in the water column with a vertical attenuation described by a power-law flux profile (Martin et al., 1987),

$$J^{\text{wc}}_{\text{rem}}(x,y,z) = \frac{\partial}{\partial z}\left((1-\sigma_{\text{DON}})\int_{z=z_c}^{z=0} J_{\text{prod}}(x,y,z)dz\left(\frac{z}{z_c}\right)^{-b}\right) \tag{A5}$$

Whatever PON is not remineralized in the water column is remineralized in the sediments ($J^{\text{sed}}_{\text{rem}}$) within that same vertical column. In the process of generating the coarse model grid, many areas that would normally be partially covered by land or have some sediment interface, such as continental shelves and islands, are completely covered over in water. We use a parameterization to account for these areas, so that remineralization in the sediments occurs not only in the last wet grid cell in each vertical column, but is distributed within the column in accordance with the fraction of each grid cell that is covered by a shallower land area. This fraction is determined by interpolating a high resolution bottom topography (ETOPO2v2) to the model grid.

Like production, nitrogen fixation occurs in the top two model layers. The local nitrogen fixation rate is given by

$$J_{\text{fix}} = F_o \times e^{-NO_3/\lambda} \times e^{(T-T_{\max})/T_o} \times \frac{I}{I+K_I} \times \frac{Fe}{Fe+K_{Fe}}, \tag{A6}$$

where F_o is the maximum nitrogen fixation rate. This parameterization takes into account the important environmental controls on fixation, including the inhibition of fixation at high NO_3 concentrations (Holl and Montoya, 2005), and the need for warm

BGD
9, 14013–14052, 2012

seawater temperatures (T) and adequate light (I) and iron (Fe) supply (e.g. Monteiro et al., 2011). Iron is not modeled explicitly, but rather we use a modeled dust deposition field (Mahowald et al., 2006) as a proxy for its availability (e.g. Somes et al., 2010). The surface irradiance I is derived from International Satellite Cloud Climatology Project-C1 data (Zhang et al., 2004).

Of all the newly fixed organic matter, a fraction ϕ_e is routed to the PON pool and remineralizes in the water-column (J^{wc}_{fix}) and sediments (J^{sed}_{fix}), following the same formulation as regular organic matter (Eq. A5). Another fraction $\phi_d = \phi_e \times \sigma_{DON}/(1-\sigma_{DON})$ is routed to the DON pool (J^{DON}_{fix}) and remineralizes following the first-order kinetics for DON remineralization. The remaining fraction $(1-\phi_e-\phi_d)$ remineralizes immediately in the surface layers where fixation occurs. Thus the individual fixation terms in Eqs. (A1) and (A2) are

$$J^{NO_3}_{fix} = (1-\phi_e-\phi_d)J_{fix}, \qquad z \geq z_c \tag{A7}$$

$$J^{NO_3}_{fix} = J^{wc}_{fix} + J^{sed}_{fix}, \qquad z < z_c \tag{A8}$$

$$J^{DON}_{fix} = \phi_d J_{fix}, \qquad z \geq z_c. \tag{A9}$$

Denitrification in the water-column occurs wherever local observed O_2 levels fall below a critical level ($O_{2,crit}$) representing the threshold at which denitrification replaces oxic respiration as the dominant pathway of organic matter degradation,

$$J_{wcd} = r_{N_{denit}:N_{org}} \times \left(J^{wc}_{rem} + J^{wc}_{fix} + \frac{1}{\tau_{DON}} DON \right) \iff O_{2,obs} < O_{2,crit} \tag{A10}$$

where $r_{N_{denit}:N_{org}}$ represents the ratio of moles NO_3 used to respire 1 mol of organic nitrogen. The "if and only if" $\iff$ statement is handled by creating a mask from the observed monthly climatology of oxygen concentrations (Garcia et al., 2010b) after applying the correction suggested by Bianchi et al., 2012 using the procedure described by DeVries et al. (2012).

BGD
9, 14013–14052, 2012

Benthic denitrification is parameterized as a function of the rate of organic matter respiration in the sediments,

$$J_{sd} = F \times (J^{sed}_{rem} + J^{sed}_{fix}) \quad \text{(A11)}$$

where F is a function that accounts for enhanced sedimentary denitrification rates under low-oxygen and high-nitrate conditions (Middelburg et al., 1996),

$$F = a_0 + a_1 F_{O_2} + a_2 F_{NO_3} + a_3 F_{O_2} F_{NO_3}, \quad \text{(A12)}$$

$$F_{O_2} = \tanh\left(\frac{C_{O_2} - O_2}{K_{O_2}} + 1\right), \quad \text{(A13)}$$

$$F_{NO_3} = \frac{NO_3}{NO_3 + K_{NO_3}}, \quad \text{(A14)}$$

where C_{O_2}, K_{O_2} and K_{NO_3} are parameters governing the oxygen and nitrate dependence of sedimentary denitrification.

The coupled system of non-linear Eqs. (A1)–(A2) for NO_3 and DON are solved using Newton's method, which produces convergence to an equilibrium state orders of magnitude faster than traditional time-stepping techniques (Kwon and Primeau, 2006). Fast convergence to an equilibrium solution is necessary for application in the inverse model, which requires $\mathcal{O}$ (10^3) runs of the forward model to converge to a solution.

The governing equations for $^{15}NO_3$ and DO^{14}N are the same as Eqs. (A1)–(A2) except that a fractionation factor α representing the discrimination of chemical reactions toward the lighter isotope is introduced in each term that involves a chemical reaction (e.g. Deutsch et al., 2004). Generically, the reaction rate (J_{reac}) for ^{15}N is related to the reaction rate for ^{14}N by

$$J^{^{15}NO_3}_{reac} = \alpha \frac{^{15}NO_3}{^{14}NO_3} J^{^{14}NO_3}_{reac}. \quad \text{(A15)}$$

BGD
9, 14013–14052, 2012

This fractionation effect is taken into account in the uptake of NO_3 to form organic N (J_{prod}), the remineralization of organic N by denitrifying bacteria in the water column (J_{wcd}) and the sediments (J_{sd}), and the fixation of atmospheric N_2 (J_{fix}). The isotopic enrichment factor for a reaction is given by $\epsilon = (\alpha - 1) \times 1000$.

Given the steady-state solution for NO_3 and DON obtained from solving Eqs. (A1)–(A2), and making the approximation $^{14}NO_3 \equiv NO_3$ and $DO^{14}N \equiv DON$, the equations for $^{15}NO_3$ and $DO^{15}N$ can be cast in terms of a coupled linear system of equations for the isotopic ratios

$$R_{NO_3} = \frac{^{15}NO_3/^{14}NO_3}{R_{std}}, \tag{A16}$$

$$R_{DON} = \frac{DO^{15}N/DO^{14}N}{R_{std}}, \tag{A17}$$

where R_{std} is the isotopic ratio of atmospheric N_2, which we take to be 1 for convenience. The resulting set of coupled linear equations can be solved by direct matrix inversion. In places where NO_3 concentrations are very low (close to zero) we find that the ratio R_{NO_3} can become ill-defined, leading to noise in the model-simulated R_{NO_3} distribution. For this reason, we neglect R_{NO_3} values above 200 m depth, where very low NO_3 can occur, when comparing the modeled and observed $\delta^{15}NO_3$ values in the inverse model (see below). We find that a similar problem occurs where DON concentrations are close to zero, which occurs in many places in the interior ocean. These points can cause an ill-conditioned (nearly singular) matrix when inverting for the modeled R_{NO_3} and R_{DON} values. We find that this problem is eliminated when we set all values where DON $< \gamma$ to γ, where γ is a small number (we used 10^{-4} μM). This does not affect the modeled R_{NO_3} values.

When comparing modeled to observed isotopic ratios for NO_3, we convert observed $\delta^{15}NO_3$ values to R_{NO_3} values using the relationship $\delta^{15}NO_3 = (R_{NO_3} - 1) \times 1000$.

BGD
9, 14013–14052, 2012

Appendix B

Inverse model description

The procedure by which the model is fit to observed N^* and $\delta^{15}NO_3$ involves two steps. In the first step, the model circulation and air-sea fluxes are adjusted to minimize the misfit between modeled and observed temperature, salinity, radiocarbon, and phosphate distributions. This procedure follows that outlined in DeVries and Primeau (2011) except that here we use a higher resolution model grid (2° horizontal resolution with 24 unevenly-spaced vertical levels) and we include phosphate observations from the 2009 World Ocean Atlas gridded database (Garcia et al., 2010a) in the set of observations to be reproduced by the model. The cycling of phosphate and dissolved organic phosphorus (DOP) are both explicitly modeled, following the same sets of equations described for the nitrogen cycle, except that the fixation and denitrification terms are of course not included. We include the depth attenuation coefficient b for particulate organic phosphate (POP) remineralization as an additional control parameter of the model to be determined as part of the optimization. Two additional parameters, σ_{DOP} and τ_{DOP} are needed for the model, but these cannot be determined as part of the optimization because DOP data is not included in the set of observational constraints. Rather, we specify σ_{DOP} and τ_{DOP} based on values determined in previous studies. In one model we specify $\sigma_{DOP} = 2/3$ and $\tau_{DOP} = 1/2$ yr (Najjar and Orr, 1998), and in another model we specify $\sigma_{DOP} = 1/2$ and $\tau_{DOP} = 2$ yr (Schlitzer, 2002).

The relative error of model state variables in this first step of the optimization is 0.8 for temperature, 0.8 for salinity, 0.65 for $\Delta^{14}C$, and 0.75 for phosphate in the case that $\sigma = 1/2$ and $\tau_{DOP} = 2$ yr (0.78 in the case that $\sigma_{DOP} = 2/3$ and $\tau_{DOP} = 1/2$ yr). Relative errors of about one indicate that the model-data residuals are distributed according to the prior estimated error covariance for the global gridded data sets (c.f. DeVries and Primeau, 2011).

BGD
9, 14013–14052, 2012

The circulation found in step one of the optimization is then taken offline and used in the nitrogen cycle simulation. Most of the parameters of the nitrogen cycle model (Eqs. A1–A17) are included as control parameters in this step of the inversion (Table B1). The exceptions are the depth attenuation coefficient for PON remineralization b, which is fixed at the value found in step one of the inversion; the isotopic enrichment factors for nitrogen fixation (ϵ_{fix}), benthic denitrification (ϵ_{b}), and assimilation of nitrate to form organic matter (ϵ_{up}), which are fixed at various values in different model configurations; and the fraction of organic nitrogen routed to the DON pool (σ_{DON}), which is fixed at either σ_{DOP} or $0.5\sigma_{\mathrm{DOP}}$ depending on the model configuration. The values of ϵ_{b}, ϵ_{fix}, ϵ_{up}, and σ_{DON} used in the different model configurations are given in Sect. 2.2.

In total, there are 21 parameters that are iteratively adjusted to find the optimal solution (Table B1). The adjustable parameters include 6 parameters controlling the rate and spatial pattern of N fixation (F_o, λ, T_o, K_I, K_{Fe}, ϕ_e); 6 parameters controlling the rate and spatial pattern of water-column denitrification ($O_{2,\mathrm{crit}}$ and $r_{\mathrm{N_{denit}:N_{org}}}$ are allowed to vary separately in the Indian Ocean, the South Pacific, and the North Pacific); 7 parameters controlling the rate and spatial pattern of benthic denitrification ($a_0 - a_3$, $C_{\mathrm{O_2}}$, $K_{\mathrm{O_2}}$, $K_{\mathrm{NO_3}}$); the timescale for remineralization of DON (τ_{DON}); and the enrichment factor for water-column denitrification (ϵ_{wcd}).

The optimal solution is defined as the set of control parameters that minimize a quadratic cost function measuring the misfit between modeled and observed N^*, between modeled and observed $\delta^{15}\mathrm{NO_3}$, and between the values of optimal parameters and their prior estimated values (Table B1). Each term in the cost function (for N^*, $\delta^{15}\mathrm{NO_3}$, and model parameters) is normalized by its estimated uncertainty and the number of elements in each vector. For N^* we choose a uniform uncertainty of $1\,\mathrm{mmol\,m^{-3}}$ on the model grid, and for $\delta^{15}\mathrm{NO_3}$ we use a uniform uncertainty of 1 ‰ on the model grid. Uncertainties for the model parameters are chosen to be as large as possible while still allowing the model to converge to a solution (Table B1). This choice is made so that the primary factor controlling the final value of model parameters is the constraints provided by the N^* and $\delta^{15}\mathrm{NO_3}$ observations.

BGD
9, 14013–14052, 2012

The optimization procedure takes an initial guess at the set of control parameters and iteratively adjusts the parameters to find the minimum of the cost function using a quasi-Newton algorithm. The algorithm typically takes several hundred iterations to find a suitable minimum (defined where the gradient of the cost function with respect to the parameters is less than 10^{-3}). This requires $\mathcal{O}$ (10^3) simulations, each of which necessitates computing the steady-state solution to the model equations. This large number of simulations is made possible by applying Newton's method to the non-linear nitrogen cycle equations, which allows rapid convergence to a steady-state solution.

Table B1 compiles the list of control parameters of the inverse model, their initial guesses and their final values. The initial guesses for parameter values were set by published estimates where available, and by hand-tuning to achieve rough consistency with observations for parameters without a published estimate. The final (post-optimization) parameter values are the mean of the values at the end of each of the 48 different optimizations (using different values of ϵ_{fix}, ϵ_{b}, and σ_{DON}), and the uncertainty is the standard deviation of each parameter in this set of 48 optimal solutions.

Acknowledgements. Funding for this research was provided by NSF grant OCE-1131548. F. Primeau acknowledges support from NSF grant OCE-1131768.

References

Altabet, M. A.: Constraints on oceanic N balance/imbalance from sedimentary ^{15}N records, Biogeosciences, 4, 75–86, doi:10.5194/bg-4-75-2007, 2007. 14016, 14025, 14029

Anderson, L. A. and Sarmiento, J. L.: Refield ratios of remineralization determined by nutrient data analysis, Global Biogeochem. Cy., 8, 65–80, 1994. 14024, 14025, 14049

Barford, C. C., Montoya, J. P., Altabet, M. A., and Mitchell, R.: Steady-state nitrogen isotope effects of N_2 and N_2O production in *Paracoccus denitrificans*, Appl. Environ. Microbiol., 65, 989–994, 1999. 14015, 14044

BGD

9, 14013–14052, 2012

Bianchi, D., Dunne, J. P., Sarmiento, J. L., and Galbraith, E. D.: Data-based estimates of suboxia, denitrification, and N_2O production in the ocean and their sensitivities to dissolved O_2, Global Biogeochem. Cy., 26, GB2009, doi:10.1029/2011GB004209, 2012. 14018, 14022, 14023, 14032

Botev, Z., Grotowski, J., and Kroese, D.: Kernel density estimation via diffusion, Ann. Stat., 38, 2916–2957, 2010. 14046

Brandes, J. A. and Devol, A. H.: Isotopic fractionation of oxygen and nitrogen in coastal marine sediments, Geochim. Cosmochim. Acta, 61, 1793–1801, 1997. 14016

Brandes, J. A. and Devol, A. H.: A global marine-fixed nitrogen isotopic budget: implications for Holocene nitrogen cycling, Global Biogeochem. Cy., 16, 1120, doi:10.1029/2001GB001856, 2002. 14015, 14016, 14023, 14025, 14027, 14029

Carpenter, E. J., Harvey, H. R., Fry, B., and Capone, D. G.: Biogeochemical tracers of the marine cyanobacterium *Trichodesmium*, Deep Sea Res. Pt. I, 44, 27–38, 1997. 14016

Codispoti, L. A.: An oceanic fixed nitrogen sink exceeding 400 $Tg\,N\,a^{-1}$ vs the concept of homeostasis in the fixed-nitrogen inventory, Biogeosciences, 4, 233–253, doi:10.5194/bg-4-233-2007, 2007. 14015, 14029

Codispoti, L. A., Brandes, J. A., Christensen, J. P., Devol, A. H., Naqvi, S. W. A., Paerl, H. W., and Yoshinari, T.: The oceanic fixed nitrogen and nitrous oxide budgets: moving targets as we enter the anthropocene, Sci. Mar., 65, 85–105, 2001. 14015, 14028

Codispoti, L. A., Yoshinari, T., and Devol, A. H.: Suboxic respiration in the oceanic water column, in: Respiration in Aquatic Ecosystems, edited by: del Giorgio, P. A. and le B. Williams, P. J., Oxford Univ. Press, New York, 225–247, 2005. 14044

De Pol Holz, R., Robinson, R. S., Hebbeln, D., Sigman, D. M., and Ulloa, O.: Controls on sedimentary nitrogen isotopes along the Chile margin, Deep-Sea Res. Pt. II, 56, 1100–1112, 2009. 14020

Deutsch, C., Sigman, D. M., Thunell, R. C., Meckler, A. N., and Haug, G. H.: Isotopic constraints on glacial-interglacial changes in the oceanic nitrogen budget, Global Biogeochem. Cy., 18, GB4012, doi:10.1029/2003GB002189, 2004. 14016, 14025, 14029, 14033

Deutsch, C., Sarmiento, J. L., Sigman, D. M., Gruber, N., and Dunne, J. P.: Spatial coupling of nitrogen inputs and losses in the global ocean, Nature, 445, 163–167, 2007. 14029

Devol, A. H. and Christensen, J. P.: Benthic fluxes and nitrogen cycling in sediments of the continental margin of the Eastern North Pacific, J. Mar. Res., 51, 345–372, 1993. 14015

BGD
9, 14013–14052, 2012

Devol, A. H., Codispoti, L. A., and Christensen, J. P.: Summer and winter denitrification rates in Western arctic shelf sediments, Cont. Shelf Res., 17, 1029–1050, 1997. 14015

DeVries, T. and Primeau, F.: Dynamically- and observationally-constrained estimates of water-mass distributions and ages in the global ocean, J. Phys. Oceanogr., 41, 2381–2401, 2011. 14017, 14035

DeVries, T., Deutsch, C., Primeau, F., Chang, B., and Devol, A.: Global rates of water-column denitrification derived from nitrogen gas measurements, Nat. Geosci., 5, 547–550, 2012. 14015, 14017, 14022, 14029, 14032

DiFiore, P. J., Sigman, D. M., and Dunbar, R. B.: Upper ocean nitrogen fluxes in the Polar Antarctic Zone: constraints from the nitrogen and oxygen isotopes of nitrate, Geochem. Geophy. Geosy., 10, Q11016, doi:10.1029/2009GC002468, 2009. 14020

Garcia, H. E., Locarnini, R. A., Boyer, T. P., Antonov, J. I., Zweng, M. M., Baranova, O. K., and Johnson, D. R.: Vol. 4: Nutrients (phosphate, nitrate, silicate), in: World Ocean Atlas 2009, NOAA Atlas NESDIS 71, edited by: Levitus, S., US Government Printing Office, Washington, DC, 2010a. 14017, 14019, 14030, 14035

Garcia, H. E., Locarnini, R. A., Boyer, T. P., Antonov, J. I., Zweng, M. M., Baranova, O. K., and Johnson, D. R.: Vol. 3: Dissolved oxygen, apparent oxygen utilization, and oxygen saturation, in: World Ocean Atlas 2009, NOAA Atlas NESDIS 68, edited by: Levitus, S., US Government Printing Office, Washington, DC, 2010b. 14018, 14032

Grosskopf, T., Mohr, W., Baustian, T., Schunck, H., Gill, D., Kuypers, M. M. M., Lavik, G., Schmitz, R. A., Wallace, W. R., and LaRoche, J.: Doubling of marine dinitrogen-fixation rates based on direct measurements, Nature, 488, 361–364, doi:10.1038/nature11338, 2012. 14029

Gruber, N.: The marine nitrogen cycle: Overview of distributions and processes, in: Nitrogen in the Marine Environment, edited by: Capone, D. G., Bronk, D. A., Mulholland, M. R., and Carpenter, E. J., Elsevier, Amsterdam, 1–50, 2008. 14015

Gruber, N. and Galloway, J. N.: An Earth-system perspective of the global nitrogen cycle, Nature, 451, 293–296, 2008. 14023

Gruber, N. and Sarmiento, J.: Global patterns of marine nitrogen fixation and denitrification, Global Biogeochem. Cy., 11, 235–266, 1997. 14015

Gruber, N. and Sarmiento, J.: Biogeochemical/physical interactions in elemental cycles, in: The Sea: Biological-Physical Interactions in the Oceans, edited by: Robinson, A. R., McCarthy, J. J., and Rothschild, B. J., John Wiley and Sons, New York, 337–399, 2002. 14015

BGD
9, 14013–14052, 2012

Hansell, D. A., Olson, D. B., Dentener, F., and Zamora, L. M.: Assessment of excess nitrate development in the Subtropical North Atlantic, Mar. Chem., 106, 562–579, 2007. 14030

Holl, C. M. and Montoya, J. P.: Interactions between nitrate uptake and nitrogen fixation in continuous cultures of the marine diazotroph *Trichodesmium* (cyanobacteria), J. Phycol., 41, 1178–1183, 2005. 14031, 14044

Knapp, A. N., Difiore, P. J., Deutsch, C., Sigman, D. M., and Lipschultz, F.: Nitrate isotopic composition between Bermuda and Puerto Rico: implications for N_2 fixation in the Atlantic Ocean, Global Biogeochem. Cy., 22, GB3014, doi:10.1029/2007GB003107, 2008. 14021, 14030

Kwon, E. Y. and Primeau, F.: Optimization and sensitivity study of a biogeochemistry ocean model using an implicit solver and in situ phosphate data, Global Biogeochem. Cy., 20, GB4009, doi:10.1029/2005GB002631, 2006. 14033

Laursen, A. E. and Seitzinger, S. P.: The role of denitrification in nitrogen removal and carbon mineralization in Mid-Atlantic bight sediments, Con. Shelf Res., 22, 1397–1416, 2002. 14015

Lehmann, M. F., Sigman, D. M., and Berelson, W. M.: Coupling the $^{15}N/^{14}N$ and $^{18}/^{16}O$ of nitrate as a constraint on benthic nitrogen cycling, Mar. Chem., 88, 1–20, doi:10.1016/j/marchem.2004.02.001, 2004. 14016

Lehmann, M. F., Sigman, D. M., McCorkle, D. C., Granger, J., Hoffman, S., Cane, G., and Brunelle, D. G.: The distribution of nitrate $^{15}N/^{14}N$ in marine sediments and the impact of benthic nitrogen loss on the isotopic composition of oceanic nitrate, Geochim. Cosmochim. Acta, 71, 5384–5404, doi:10.1016/j.gca.2007.07.025, 2007. 14016

Liu, K. K.: Geochemistry of inorganic nitrogen compounds in two marine environments: the Santa Barbara Basin and the ocean off Peru, PhD thesis, University of California, Los Angeles, CA, 1979. 14020

Macko, S. A., Fogel, M. L., Hare, P. E., and Hoering, T. C.: Isotope fractionation of nitrogen and carbon in the synthesis of amino acids by microorganisms, Chem. Geol. Isot. Geosci. Sect., 65, 72–92, 1987. 14016

Mahowald, N. M., Muhs, D. R., Levis, S., Rasch, P. J., Yoshioka, M., Zender, C. S., and Luo, C.: Change in atmospheric mineral aerosols in response to climate: last glacial period, preindustrial, modern, and doubled carbon dioxide climates, J. Geophys. Res., 111, D10202, doi:10.1029/2005JD006653, 2006. 14032

Martin, J., Knauer, G., Karl, D., and Broenkow, W.: VERTEX: carbon cycling in the Northeast Pacific, Deep Sea Res., 34, 267–285, 1987. 14018, 14031

BGD
9, 14013–14052, 2012

Middelburg, J., Soetart, K., Herman, P. M. J., and Heip, C. H. R.: Denitrification in marine sediments: a model study, Global Biogeochem. Cy., 10, 661–673, 1996. 14015, 14022, 14023, 14033

Monteiro, F. M., Dutkeiwicz, S., and Follows, M. J.: Biogeographical controls on the marine nitrogen fixers, Global Biogeochem. Cy., 25, GB2003, doi:10.1029/2010GB003902, 2011. 14032

Najjar, R. and Orr, J.: Design of OCMIP-2 simulations of chlorofluorocarbons, the solubility pump and common biogeochemistry, online document, available at: http://www.ipsl/jussieu.fr/OCMIP/phase2/simulations/design.ps, 1998. 14017, 14035

Paulmier, A., Kriest, I., and Oschlies, A.: Stoichiometries of remineralisation and denitrification in global biogeochemical ocean models, Biogeosciences, 6, 923–935, doi:10.5194/bg-6-923-2009, 2009. 14044

Primeau, F., Holzer, M., and DeVries, T.: Southern Ocean nutrient trapping and the efficiency of the biological pump, J. Geophys. Res., in review, 2012. 14046

Rafter, P. A., Sigman, D. M., Charles, C. D., Kaiser, J., and Haug, G. H.: Subsurface Tropical Pacific nitrogen isotopic composition of nitrate: biogeochemical signals and their transport, Global Biogeochem. Cy., 26, GB1003, doi:10.1029/2010GB003979, 2012. 14020

Rao, A. M. F., McCarthy, M. J., Gardner, W. S., and Jahnke, R. A.: Respiration and denitrification in permeable continental shelf deposits on the South Atlantic Bight: rates of carbon and nitrogen cycling from sediment column experiments, Cont. Shelf Res., 27, 1801–1819, 2007. 14015

Schlitzer, R.: Carbon export fluxes in the Southern Ocean: results from inverse modeling and comparison with satellite-based estimates, Deep-Sea Res. Pt. II, 49, 1623–1644, 2002. 14035

Seitzinger, S., Bohlke, J. K., Bouwman, A. F., Lowrance, R., Peterson, B., Tobias, C., and Drecht, G. V.: Denitrification across landscapes and waterscapes: a synthesis, Ecol. Appl., 16, 2064–2090, 2006. 14022

Somes, C. J., Schmittner, A., Galbraith, E. D., Lehmann, M. F., Altabet, M. A., Montoya, J. P., Letelier, R. M., Mix, A. C., Bourbonnais, A., and Eby, M.: Simulating the global distribution of nitrogen isotopes in the ocean, Global Biogeochem. Cy., 24, GB4019, doi:10.1029/2009GB003767, 2010. 14016, 14019, 14020, 14027, 14032

BGD
9, 14013–14052, 2012

Yoshikawa, C., Nakatsuka, T., and Kawahata, H.: Transition of low-salinity water in the Western Pacific Warm Pool recorded in the nitrogen isotopic ratios of settling particle, Geophys. Res. Letters, 32, L14615, doi:10.1029/2005GL023103, 2005. 14020

Yoshikawa, C., Nakatsuka, T., and Wakatsuchi, M.: Distribution of N^* in the Sea of Okhotsk and its use as a biogeochemical tracer of the Okhotsk Sea Intermediate Water formation process, J. Marine Syst., 63, 49–62, 2006. 14016, 14020

Zhang, Y., Rossow, W. B., Lacis, A. A., Oinas, V., and Mishchenko, M. I.: Calculation of radiative fluxes from the surface to the top of atmosphere based on ISCCP and other global data sets: refinements of the radiative transfer model and the input data, J. Geophys. Res., 109, D19105, doi:10.1029/2003JD004457, 2004. 14032

BGD

9, 14013–14052, 2012

Table 1. Integrated denitrification rates by ocean basin. Median rate is given, with range in parentheses. The range includes uncertainty due to uncertainty in the isotopic enrichment factors of fixation and benthic denitrification, and in the parameterization of dissolved organic matter. Southern Ocean is south of 34° S. Global rates also include contribution from benthic denitrification in the Arctic Ocean and the Mediterranean Sea.

Region	Water-column denitrification (W) ($TgN\,yr^{-1}$)	Benthic denitrification (B) ($TgN\,yr^{-1}$)	Total denitrification ($TgN\,yr^{-1}$)
Atlantic	0	16 (12–25)	16 (12–25)
Pacific	50 (41–63)	42 (25–68)	92 (66–130)
Indian	10 (9–14)	20 (13–29)	31 (22–41)
Southern Ocean	0	26 (16–43)	26 (26–43)
Global	60 (50–77)	109 (71–168)	170 (121–242)

BGD
9, 14013–14052, 2012

Table B1. Prior (pre-optimization) and posterior (post-optimization) values of the control parameters, and associated uncertainties. Prior uncertainties are 1 standard deviation of a normal distribution.

Parameter	Units	Prior value	Prior uncertainty	Posterior value	Posterior uncertainty
F_o	$\mathrm{mmol\,N\,m^{-3}\,yr^{-1}}$	1.5	5	1.5	0.2
λ	$\mathrm{mmol\,N\,m^{-3}}$	10[a]	5	9.5	0.4
K_I	$\mathrm{W\,m^{-2}}$	25	10	24.6	0.3
T_o	°C	20	10	21.3	1.9
K_{Fe}	$\mathrm{g\ dust\ m^{-2}\,yr^{-1}}$	0.2	0.5	0.03	0.03
ϕ_e	none	0.15	0.2	0.13	0.04
$O_{2,\mathrm{crit}}$ Ar. Sea	$\mu\mathrm{M\ O_2}$	4[b]	8	1.1	0.2
$O_{2,\mathrm{crit}}$ ETSP	$\mu\mathrm{M\ O_2}$	4[b]	8	5.0	0.5
$O_{2,\mathrm{crit}}$ ETNP	$\mu\mathrm{M\ O_2}$	4[b]	8	2.8	0.3
$r_{N_{\mathrm{wcd}}:N_{\mathrm{org}}}$ Ar. Sea	$\mathrm{mol\,NO_3\,(mol\,N_{org})^{-1}}$	7[c]	3	7.0	0.1
$r_{N_{\mathrm{wcd}}:N_{\mathrm{org}}}$ ETSP	$\mathrm{mol\,NO_3\,(mol\,N_{org})^{-1}}$	7[c]	3	7.2	0.1
$r_{N_{\mathrm{wcd}}:N_{\mathrm{org}}}$ ETNP	$\mathrm{mol\,NO_3\,(mol\,N_{org})^{-1}}$	7[c]	3	6.0	0.1
a_0	$\mathrm{mol\,NO_3\,(mol\,N_{org})^{-1}}$	0.1	10	0.2	0.1
a_1	$\mathrm{mol\,NO_3\,(mol\,N_{org})^{-1}}$	0.1	10	1.6	1.1
a_2	$\mathrm{mol\,NO_3\,(mol\,N_{org})^{-1}}$	0.1	10	0.6	0.5
a_3	$\mathrm{mol\,NO_3\,(mol\,N_{org})^{-1}}$	0.1	10	1.4	1.6
C_{O_2}	$\mu\mathrm{M\ O_2}$	50	100	46	6
K_{O_2}	$\mu\mathrm{M\ O_2}$	50	100	31	26
K_{NO_3}	$\mathrm{mmol\,N\,m^{-3}}$	40	40	32	15
ϵ_w	‰	25[d]	5	24	2.6
τ_{DON}	yr	$2\tau_{\mathrm{DOP}}$	$5\tau_{\mathrm{DOP}}$	3.0[e]	2.4

[a] Holl and Montoya (2005)
[b] Codispoti et al. (2005)
[c] Paulmier et al. (2009)
[d] Barford et al. (1999)
[e] Depends on value of σ_{DON} used and varies from 0.4 ± 0.1 yr for $\sigma_{\mathrm{DON}} = 2/3$, to 6.6 ± 0.8 yr for $\sigma_{\mathrm{DON}} = 1/4$.

BGD
9, 14013–14052, 2012

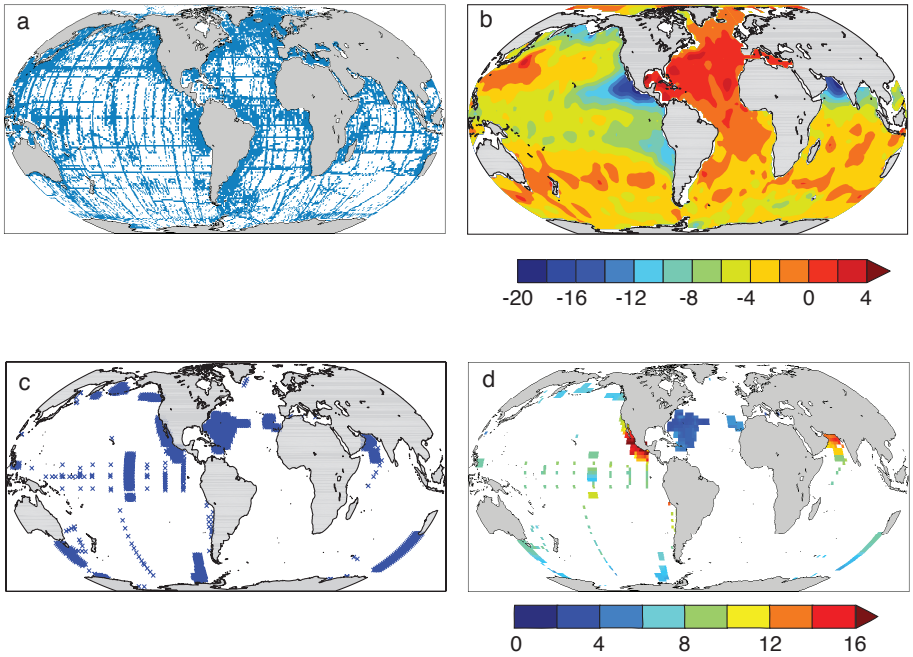

Fig. 1. (a) Locations of N^* data (all depths), **(b)** objectively mapped N^* (μM) for the depth interval 200–550 m, **(c)** locations of N isotope data (all depths), and **(d)** $\delta^{15}NO_3$ concentrations (‰) averaged over the depth interval 200–550 m.

BGD
9, 14013–14052, 2012

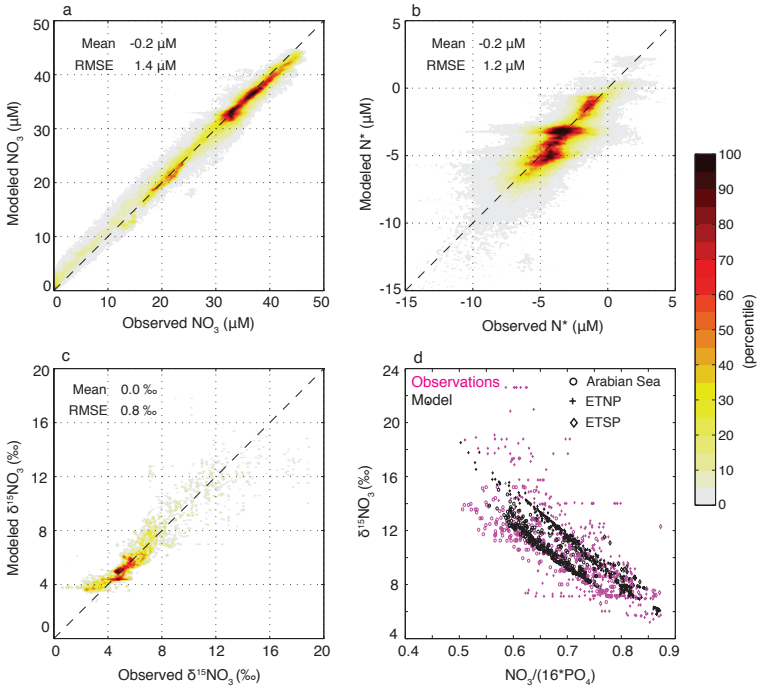

Fig. 2. (a–c) Joint distribution function for the gridbox-volume-weighted observed and modeled tracer concentrations. The joint distribution function was estimated using the kernel density estimation method described in Botev et al. (2010) with a modification to account for the volume of the model grid boxes (Primeau et al., 2012). Printed on each plot is the gridbox-volume-weighted mean model-data difference and the gridbox-volume-weighted root mean squared error. **(d)** Rayleigh curve showing modeled and observed $\delta^{15}NO_3$ vs. relative nitrate consumption for all locations with $\delta^{15}NO_3$ observations and O_2 concentrations less than 20 µM. Symbols in **(d)** distinguish different oceanic regions. Results plotted here are averages of the optimal solutions under all 48 different model configurations.

BGD
9, 14013–14052, 2012

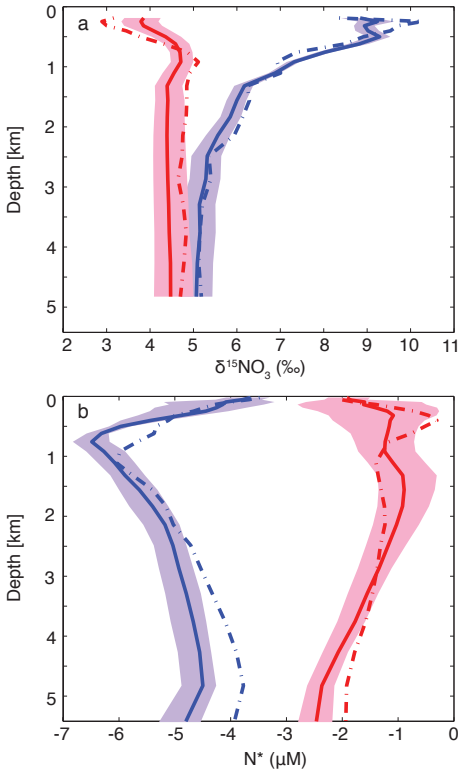

Fig. 3. (a) Depth profiles of modeled (solid curve) and observed (dashed curve) $\delta^{15}NO_3$ for the Indo-Pacific (blue) and Atlantic (red) basins. Depth averages are taken over all model grid cells for which there is at least one $\delta^{15}NO_3$ observation. There are no observations below 4800 m, and observations at depths shallower than 200 m are not used to constrain the model. **(b)** Depth profiles of modeled and observed N^* for the Indo-Pacific and Atlantic basins. Shading around model mean depth profile is the range from all model solutions.

BGD
9, 14013–14052, 2012

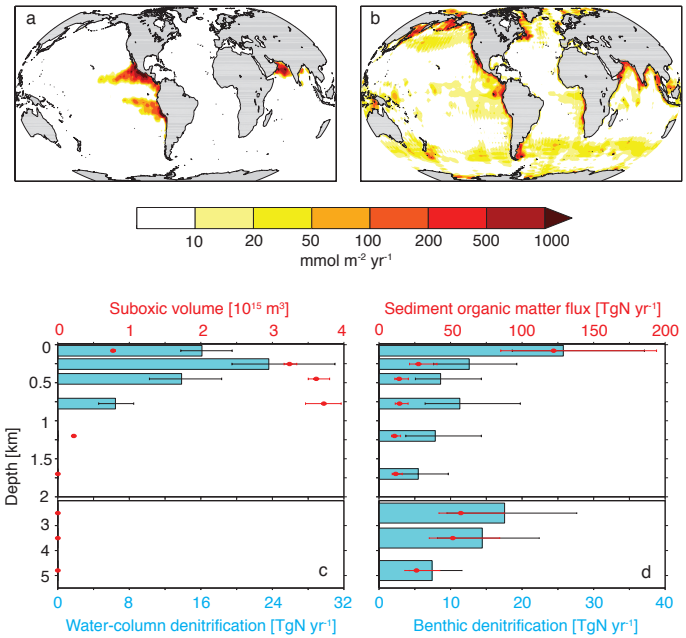

Fig. 4. Depth-integrated rate of water column denitrification, **(b)** depth-integrated rate of benthic denitrification, **(c)** water-column denitrification rate (blue bars with black error bars, lower axis) and suboxic volume (red circles with red error bars, upper axis) integrated over various depth intervals (0–160 m, 160–350 m, 350–550 m, 550–1000 m, 1000–1400 m, 1400–2000 m, 2000–3000 m, 3000–4000 m, and 4000–5500 m) and **(d)** benthic denitrification rate (blue bars with black error bars, lower axis) and sediment organic matter flux rate (red circles with red error bars, upper axis) integrated over the same depth intervals as in **(c)**. Note nonlinear color scale in **(a)** and **(b)**. Vertical axis stretched for top 2000 m in **(c)** and **(d)**. Median rates are given in **(a)** and **(b)**, while error bars in **(c)** and **(d)** span the full range of model predictions.

BGD
9, 14013–14052, 2012

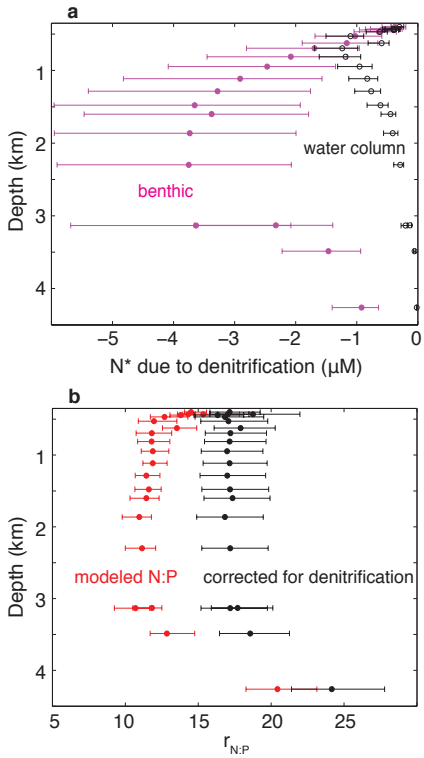

Fig. 5. (a) The depth distribution of N* due to benthic denitrification (filled magenta circles with error bars) and water-column denitrification (open black circles with error bars). The N* due to denitrification is approximated by the concentration of an idealized tracer that is lost from the ocean at a rate proportional to the rate of denitrification. **(b)** The N : P ratio of remineralized organic matter calculated according to the method of Anderson and Sarmiento (1994) using the modeled NO_3 and PO_4 fields (red circles and error bars), and the ratio after correcting for the amount of NO_3 that is lost due to denitrification (black circles with error bars). All calculations are performed on isopycnal surfaces and plotted at the mean depth of each isopycnal.

BGD
9, 14013–14052, 2012

Marine denitrification rates from a global inverse model

T. DeVries et al.

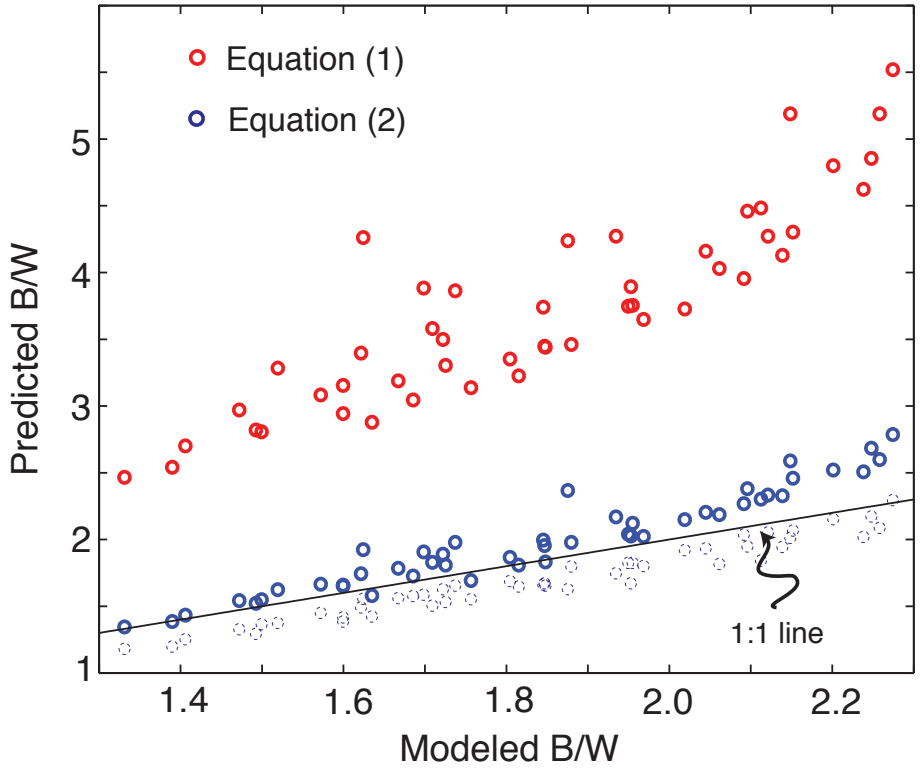

Fig. 6. Modeled ratio of benthic to water-column denitrification (B/W) compared to that predicted by a linear isotope mass balance (Eq. 1, bold red circles) and an isotope mass balance corrected for the fractional consumption of nitrate in suboxic zones (Eq. 2, bold blue circles). The faint dashed blue circles show results from Eq. (2) when the mean ocean $\delta^{15}NO_3$ is corrected for fractionation during uptake of nitrate to form organic matter.

BGD
9, 14013–14052, 2012

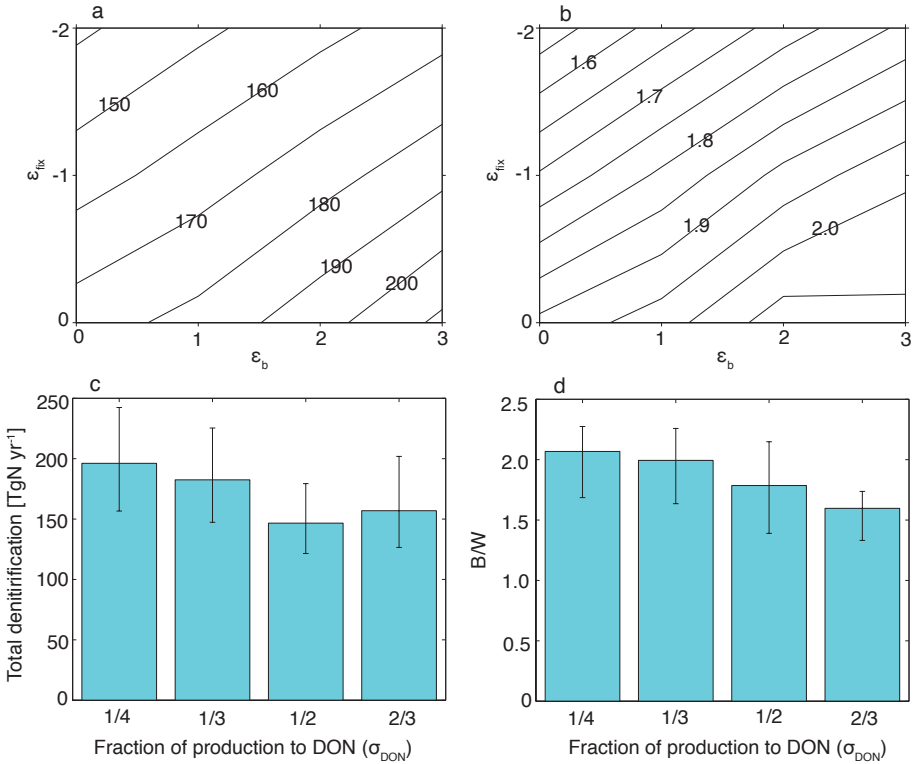

Fig. 7. (a) Globally-integrated denitrification (TgN yr^{-1}) and **(b)** ratio of benthic (B) to water-column (W) denitrification as a function of isotopic enrichment factors for nitrogen fixation (ϵ_{fix}) and benthic denitrification (ϵ_b). **(c)** Globally-integrated denitrification and **(d)** B/W as a function of the fraction of organic matter production routed to the dissolved organic nitrogen (DON) pool. Results in **(a)** and **(b)** show mean values from all model solutions, and results in **(c)** and **(d)** show median (filled bars) and range (error bars) from all model solutions.

BGD
9, 14013–14052, 2012

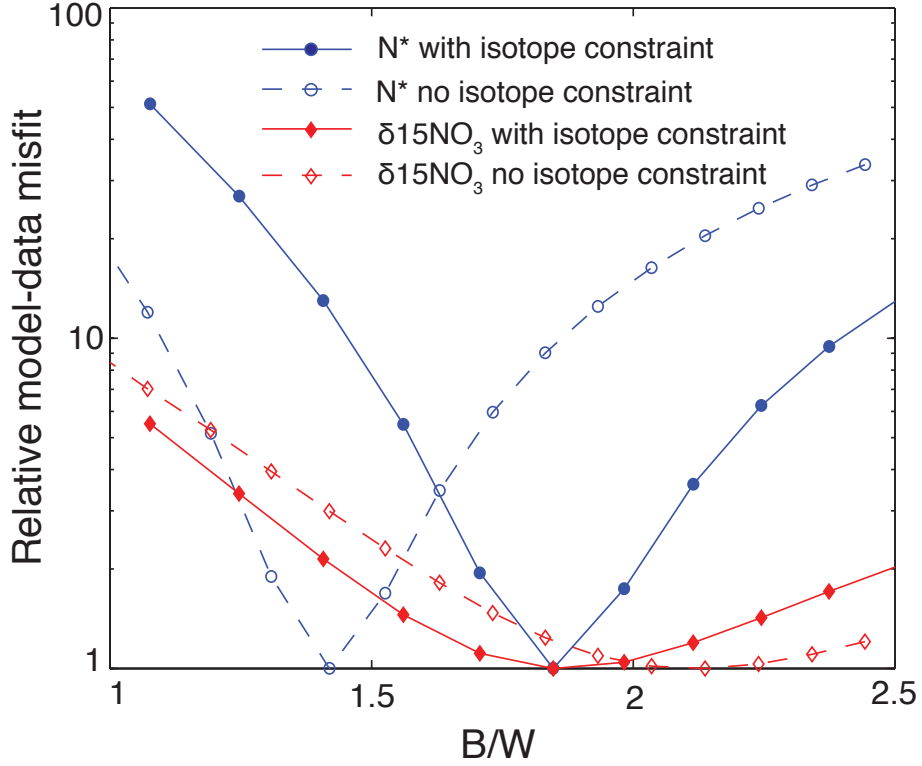

Fig. 8. Sensitivity of model-data misfit to partitioning of denitrification between sediments and water column. We start with a model solution in which only N^* is used a constraint (open symbols), and one in which both N^* and $\delta^{15}NO_3$ are used as constraints (closed symbols). We then vary B/W by adjusting the parameters determining the rate of benthic denitrification, while keeping all other parameters and the total denitrification rate constant. These experiments use the model configuration with $\epsilon_{fix} = 0$, $\epsilon_b = 0$, and $\sigma_{DON} = 1/4$.

BGD
9, 14013–14052, 2012